CORA Cork Open Research Archive
Cartlann Taighde Oscailte Chorcaí

Title	Hydrokinetic energy exploitation under combined river and tidal flow
Authors	Fouz, D. M.;Carballo, Rodrigo;Ramos, V.;Iglesias, Gregorio
Publication date	2019-05-11
Original Citation	Fouz, D. M., Carballo, R., Ramos, V. and Iglesias, G. (2019) 'Hydrokinetic energy exploitation under combined river and tidal flow', Renewable Energy, 143, pp. 558-568. doi: 10.1016/j.renene.2019.05.035
Type of publication	Article (peer-reviewed)
Link to publisher's version	http://www.sciencedirect.com/science/article/pii/S0960148119306949 - 10.1016/j.renene.2019.05.035
Rights	© 2019 Elsevier Ltd. All rights reserved. This manuscript version is made available under the CC-BY-NC-ND 4.0 license - http://creativecommons.org/licenses/by-nc-nd/4.0/
Download date	2026-11-04 11:17:06
Item downloaded from	https://hdl.handle.net/10468/8200

UCC
University College Cork, Ireland
Coláiste na hOllscoile Corcaigh

*Revised Manuscript-Clear
Click here to download Revised Manuscript-Clear: Final_manuscript_revised.docx Click here to view linked References

Hydrokinetic energy exploitation under combined river and tidal flow

D.M. Fouz[1], R. Carballo[1*], V. Ramos[2], G. Iglesias[3, 4]

[1]*Univ. de Santiago de Compostela, Área de Ingeniería Hidráulica, EPSE, Campus Univ. s/n, 27002 Lugo, Spain*

[2]*Interdisciplinary Centre of Marine and Environmental Research of the University of Porto, Terminal de Cruzeiros do Porto de Leixões, Avenida General Norton de Matos, S/N, 4450-208 Matosinhos, Portugal*

[3]*MaREI, Environmental Research Institute & School of Engineering, University College Cork, Ireland*

[4]*School of Engineering, University of Plymouth, UK*

Abstract

Hydrokinetic energy has been mainly studied in areas where the principal driver of the current is the tide. However, in certain areas river discharges play also a principal role. The exploitation of the hydrokinetic resource in such areas has its own peculiarities, dictated by the combined influence of the two driving agents. The objective of this paper is to investigate the exploitation of hydrokinetic energy in the Miño Estuary, the largest estuary in NW Spain and N Portugal, with a focus on the site-specific performance of hydrokinetic energy converters (HECs) and its intra-annual variability. A state-of-the-art hydrodynamics numerical model is implemented and successfully validated based on field data. A third-generation HEC—to be more specific, the new Smart Freestream Turbine (SFT)—is considered, and its performance at the location with the greatest potential is assessed by means of: (i) site-specific efficiency, (ii) availability factor, and (iii) capacity factor. We find that, whereas the site-specific efficiency does not vary significantly, the availability and capacity factors do experience substantial intra-annual (seasonal) variability. In summer and autumn, river discharges are low, and the tide dominates the hydrokinetic resource. In contrast, during winter and spring, the river discharges significantly contribute to the resource, leading to a considerable increase in the availability and capacity factors. More generally, the results imply that in areas subject to combined fluvial and tidal influences the performance of HECs may depart significantly from that in tide-dominated areas, and this departure must be carefully weighed in assessing a project.

Keywords: hydrokinetic energy; tidal stream energy; river discharge; seasonal variability; hydrokinetic energy converter

*Corresponding author
E-mail address: rodrigo.carballo@usc.es

1. Introduction

Global warming has drawn attention to new renewable ways of energy production based on principles of efficiency and sustainability [1]. As a result, hydrokinetic energy has been postulated as one of the most promising renewable energy sources that can be developed in the medium term due to its high potential and its reduced environmental impact [2-6].

The hydrokinetic resource is the result of different factors, namely: tidal currents, ocean currents, barotropic flows resulting from river discharges and baroclinic circulation, amongst others. The viability of its exploitation requires that peak velocities attain 1-1.5 ms^{-1} [7]. As a result, estuarine areas have emerged as a promising site for the exploitation of hydrokinetic energy, primarily resulting from the action of the tide which is enhanced by the complex geometry of semi-enclosed bodies [8-10]. Nevertheless, the influence of large river discharges on the available resource and their interaction with tidal flows have not been appropriately investigated.

On the other hand, the hydrokinetic resource can be harnessed by the so-called Hydrokinetic Energy Converters (HECs). According to the International Electrotechnical Commission (IEC) criterion, HECs can be classified in five main groups [11-15]: (i) devices with horizontal axis parallel to flow, (ii) devices with horizontal axis perpendicular to flow, (iii) devices with vertical axis, (iv) hydrofoils and (v) other devices. HECs are still currently under development and, as it is the case of other marine renewables [16,17], they are expected to become more economically competitive. Recently, a new generation of HECs has been developed, the so-called third generation devices [18], designed to operate in shallow areas with relatively low velocities and reduced depths (roughly 0.7 ms^{-1} of velocity magnitude and 1 m depth) —where hydrokinetic energy exploitation was not previously considered— and allowing the reduction of the environmental impact by using a compact generation equipment.

Planning of a new hydrokinetic energy farm should rely on the selection of the optimum device-location combination, which in turn should consider several aspects [19-21], as it is the case of other marine renewables [22-24]. This is of paramount importance in shallow areas with narrow sections given that, in addition to energy production considerations, the geometry imposes

strong limitations to turbine installation and operation [25-27]. In this context, the Galician coast is characterized by a number of estuaries with complex geometry and, in some cases, substantial freshwater discharges. River Miño is the most important fluvial course in this region. Its estuary, with its main axis (Figures 1 and 2) extending over approximately 38 km [28] has a total area of about 23 km^2 and an average depth of about 2.6 m [29]. The tidal regime is purely semidiurnal, with a form factor [30] F = 0.0932 and a maximum tidal range of approximately 4.0 m (mesotidal). The estuarine circulation will be shown to be profoundly influenced by the river discharge. The annual discharge is roughly 400 m^3s^{-1}, ranging from monthly minima of 100 m^3s^{-1} to monthly maxima of 1000 m^3s^{-1}. As a result of the action of the two major hydrodynamic forcing factors (the tide and freshwater discharges) over its narrow and shallow sections, this estuary presents significant current velocities, well in excess of 1 ms^{-1}, and therefore constitutes a hotspot for hydrokinetic energy exploitation [31].

[FIGURE 1]

[FIGURE 2]

In this work, the hydrokinetic resource exploitation in the Miño Estuary is analysed by considering the installation of a Smart Freestream Turbine (SFT). For this purpose, and considering the high variability in the freshwater discharge, which may be expected to affect the intra-annual performance of the SFT, the intra-annual spatio-temporal distribution of the current velocities is computed by implementing a shallow-water numerical model. Then, by combining the velocity data obtained by the numerical model with the power curve of the device, the intra-annual energy production of SFT at three locations of interest [31] is computed (Figure 2). Finally, having determined the SFT-site combination providing the largest energy production amongst those previously selected, its performance is thoroughly analysed through a gamut of performance parameters.

This paper is structured as follows: first, in Section 2, the methodology used in this work for assessing the resource distribution and analysing the performance of the HEC selected is thoroughly described; then, in Section 3, the results are presented and discussed focusing on three main aspects: resource assessment, site selection and performance analysis; finally, in Section 4, the major findings and conclusions are presented.

2. Material and methods

2.1. Numerical model formulation

The first step prior to proposing alternatives for installing a hydrokinetic turbine is to thoroughly analyse the space-time distribution of the available resource. To this end, the Delft3D FLOW model [32] is implemented for the Miño Estuary and validated by means of field data. The model solves the Navier-Stokes equations under the shallow-water and Boussinesq assumptions coupled to the transport equation, thereby allowing the computation of both the barotropic and baroclinic circulation. The equations are solved in their 2DH form [33,34]:

$$\frac{\partial \zeta}{\partial t} + \frac{\partial\left[(d+\zeta)U\right]}{\partial x} + \frac{\partial\left[(d+\zeta)V\right]}{\partial y} = Q\,, \tag{1}$$

$$\left.\begin{aligned} \frac{\partial U}{\partial t} + U\frac{\partial U}{\partial x} + V\frac{\partial U}{\partial y} - fV &= -g\frac{\partial \zeta}{\partial x} - \frac{g}{\rho_0}\int_{-d}^{\zeta}\frac{\partial \rho'}{\partial x}dz + \frac{\tau_{sx}-\tau_{bx}}{\rho_0(d+\zeta)} + \upsilon_h\nabla^2 U \\ \frac{\partial U}{\partial t} + U\frac{\partial V}{\partial x} + V\frac{\partial V}{\partial y} + fU &= -g\frac{\partial \zeta}{\partial y} - \frac{g}{\rho_0}\int_{-d}^{\zeta}\frac{\partial \rho'}{\partial y}dz + \frac{\tau_{sy}-\tau_{by}}{\rho_0(d+\zeta)} + \upsilon_h\nabla^2 V \end{aligned}\right\}, \text{ and} \tag{2}$$

$$\frac{\partial(\zeta+d)c}{\partial t} + \frac{\partial\left[(\zeta+d)Uc\right]}{\partial x} + \frac{\partial\left[(\zeta+d)Vc\right]}{\partial y} = D_h\nabla^2 c - \lambda_d(d+\zeta)c + R\,, \tag{3}$$

where (1) represents the conservation of mass under Boussinesq's hypothesis; the pair of equations (2) express the conservation of momentum along x and y directions; and (3) is the transport equation, which is solved for temperature and salinity. In these equations ζ and d

represent the water levels and depth, respectively; u and v are the components of the velocity in the directions x and y respectively; ρ and ρ_0 express the density and reference density of sea water respectively; Q is the intensity of mass sources; f stands for the Coriolis parameter; υ_h is the horizontal eddy viscosity; τ_{bx} and τ_{by} are the shear stress components over the sea bottom, and τ_{sx} and τ_{sy} the wind stress components on the sea surface; c represents the temperature or salinity constituents; D_h is the horizontal eddy diffusivity; λ_d represents the decay processes of first-order; finally, R stands for the source term.

Regarding the spatial discretisation, the model uses the Arakawa-C grid, consisting in a staggered grid within which ζ is defined at grid cell centres, and u and v are determined at the central points of the grid cell faces. With respect to the discretisation of the horizontal advection terms, the Cyclic method is applied. Finally, temporal discretisation is carried out by using a semi-implicit alternating direction implicit (ADI) algorithm.

2.2. Numerical model implementation

The finite difference mesh is a Cartesian grid with a spatial resolution of 100 x 100 m which covers the whole estuary, including the intertidal zones and emerged areas, and extends offshore up to a water depth of approximately 100 m. In this manner the outer boundary is far enough that eventual numerical disturbances do not affect the study area (Figure 3). The model is run with a time step of 1 minute, which according to the Courant–Friedrichs–Levy criterion is sufficient to ensure numerical stability considering the mesh resolution adopted [35].

[FIGURE 3]

The bathymetry, kindly provided by Hydrographic Institute of the Navy, was complemented with a digital terrain model with a resolution of 50 x 50 m commissioned by the Galician Regional Government (Xunta de Galicia), which allowed the representation of the intertidal areas. The accurate representation of shallow areas is of key importance given the sensitivity of the hydrokinetic resource to variations in the water depth and geomorphological configuration

[36]. Figure 4 shows the bathymetry and topographic data as interpolated onto the computational grid in the study area.

[FIGURE 4]

The oceanic open boundaries comprise the north, south and west limits of the grid, along which the main harmonics [37] of the astronomical tide (Table 1) and the salinity and temperature of the oceanic waters are imposed through Dirichlet boundary conditions. The freshwater input of the River Miño is imposed at the inner estuary, defined by its total discharge along with salinity and temperature characteristics.

[TABLE 1]

Previous works [31] have shown that the discharge of the River Miño presents a markedly seasonal behaviour. On this basis, four case studies are defined based on the variability of the flow discharge as provided by the Miño-Sil Hydrographic Confederation for an average year (Table 2).

[TABLE 2]

In order to analyse the seasonal hydrodynamics, the model is used to simulate the aforementioned four seasonal scenarios by considering the average characteristics of the relevant forcing factors during each of these four periods. In addition, in order to capture the variability resulting from the tide within each case, the model is run during a 14.75 day period [33,35] (half synodic month), i.e., a complete spring-neap tidal cycle, preceded by an additional spin-up period [38].

2.3. Numerical model validation

With the aim of validating the numerical model, computed velocity measurements are compared with field data recorded by an Acoustic Doppler Current Profiler (ADCP) during a period of approximately 22 days. Before comparing computed and measured data, observed velocities are de-noised and vertically averaged by means of a Stationary Wavelet Transformation (SWT) of db10 type belonging to Daubechies family [39-42]. Figure 5 shows the comparison between simulated and measured data. Overall, the model accurately reproduces the hydrodynamics of the estuary, with a high determination coefficient, R^2=0.85. In particular, the model captures the variation induced by the action of the tide, with downstream and upstream velocities corresponding to positive and negative values, respectively, along with the flow induced by the river which leads to a significant asymmetry in the resulting currents.

[FIGURE 5]

2.4. Hydrokinetic energy resource and HEC performance assessment

The available power density from the kinetic energy of the water flowing through a vertical cross-section perpendicular to flow direction per unit of time $p_{KE}(t)$ is given by [33]:

$$p_{KE}(t) = \frac{1}{2}\rho\alpha(t)\left[V(t)\right]^3 \tag{4}$$

where ρ represents the water density; $V(t)$ is the flow velocity averaged over the section per unit of time; finally, $\alpha(t)$ is the energy coefficient which takes into account the velocity dispersions through the water column being usually set as $\alpha(t) \approx 1$ [43].

The electrical energy output of a HEC, E_e, over a period of time, T, can be obtained by integrating the power density over the period of interest as [35]:

$$E_e = \int_0^T AC_p\, p_{KE}\left(t\right) dt \tag{5}$$

where C_p is the power coefficient which represents the relationship between power available and harnessed [44]; finally, A is the swept area.

It is important to consider that the above equations (Eq. 4 and Eq. 5) are theoretical expressions. Real HECs only work within a specific range of velocities with a lower velocity threshold or cut-in, V_{ci}, and upper threshold or cut-off, V_{co} [35]. The efficiency of HECs is provided by device developers through its power curve. The main technical specifications and power curve of SFT are shown in Table 3 and Figure 6, respectively.

[TABLE 3]

[FIGURE 6]

As a result, the energy output of the SFT-site combinations selected is straightforwardly computed by combining the current velocity results obtained at the locations of interest and the power curve of the SFT. As expressed in Eq. 5 the electrical energy output, E_e, is determined by integrating the power output data with respect to time, which is computed for the four case studies, each of them covering a 14.75-day period. Annual figures are obtained by considering that the intra-seasonal resource distribution is appropriately characterized by the fortnightly period, i.e.:

$$\left(E_{e,season}\right)_i = \frac{\left(E_{e,simulation}\right)_i}{T_{simulation}} T_{season} \tag{6}$$

$$E_{e,annual} = \sum_{i=1}^{4} (E_{e,season})_i \tag{7}$$

where $(E_{e,season})_i$ is the seasonal energy production for the i season; $(E_{e,simulation})_i$ represents the energy production during the 14.75-day simulation period for the i season; $T_{simulation}$ expresses

the duration of the simulation period, i.e., 14.75 days; T_{season} stands for the duration of a natural season; finally, $E_{e,annual}$ is the annual energy output.

Based on previous works [35,45-47], three performance parameters are selected for the analysis of the SFT-site combination providing the largest amount of energy: (i) the site-specific efficiency, (ii) the availability factor and (iii) the capacity factor.

The site-specific efficiency, η_e, was defined in previous work [35] as the ratio between the electrical energy output, E_e, and the available energy at the site, E, over a reference period of time:

$$\eta_e = \frac{E_e}{E} \tag{8}$$

The availability factor, A_f, is the ratio between the operation time, t_o (during which the flow speed is between the cut-in and cut-off velocities of the HEC) and the total period considered, T [46]:

$$A_f = \frac{t_o}{T} \tag{9}$$

Finally, the capacity factor, C_f, is the ratio between the electrical energy output of a device over a given period, E_e, and the electrical energy output it would have produced, had it operated at its nominal regime during the same period [47]:

$$C_f = \frac{E_e}{TP_R} \tag{10}$$

where T is the duration of the reference period and P_R is the rated electrical power of the device.

3. Results and discussion

3.1. Resource assessment

Once validated, the numerical model can be used to compute the flow throughout the estuary. For this purpose, and in order to quantify the hydrokinetic resource and the influence of the fresh water discharge, the model is run considering the combined effect of the main forcing factors as defined in Section 2. The analysis of the results is focused on three specific sites of interest for energy exploitation: Area I in the middle estuary and Areas II and III in the inner estuary (Figure 2) [31].

Given that the aim of this work is to quantify the hydrokinetic energy production in the areas proposed—and the influence of fluvial discharges on it—the numerical model was applied to compute the flow patterns during a spring-neap tidal cycle for the four case studies defined (Section 2); the results are presented in Figures 7, 8 and 9 for Areas I, II and III, respectively. The highest velocities occur during winter, the season with the largest freshwater discharge, with a gradual and significant reduction from spring to autumn due to the reduction in freshwater discharges. The influence of the river inputs is clearly observed in winter, during which upstream velocities virtually disappear. The gradual reduction in the river discharge allows upstream velocities to develop, as is apparent from the presence of a clear second peak in each tidal cycle in summer and autumn of almost the same intensity as during the ebb.

[FIGURE 7]

[FIGURE 8]

[FIGURE 9]

From the analysis of the variations in the flow speed in the three areas selected, the following results are obtained. The largest reduction in flow speed from one season to the next, hereinafter referred to as *seasonal reduction*, occurs from winter to spring, with average values of 0.40

ms^{-1}, 0.50 ms^{-1} and 0.35 ms^{-1} in Areas I, II and III, respectively, closely followed by spring and summer seasons, with mean *seasonal reductions* of 0.20 ms^{-1}, 0.40 ms^{-1} and 0.33 ms^{-1} in Areas I, II and III, respectively. In contrast, the *seasonal reduction* from summer to autumn is almost negligible: 0.01 ms^{-1}, 0.02 ms^{-1} and 0.02 ms^{-1} for Areas I, II and III, respectively. These trends are caused by the intra-annual reductions in freshwater discharges, roughly of 450 m^3s^{-1} from winter to spring, 400 m^3s^{-1} from spring to summer, and 45 m^3s^{-1} from summer to autumn (i.e., approx. a reduction of 44%, 69% and 26%, respectively). In addition, it can be observed that the geometrical characteristics lead to a different reduction in the magnitude of the currents amongst the areas considered, the section with largest modifications being the narrowest (≈165 m).

The aforementioned seasonal variations in flow speed result in large seasonal variations in the available power density (Eq. 5). In Figure 10, the seasonal power density is plotted for the area with the greatest resource (Area II). In accordance with the seasonal distribution of fluvial contributions and resulting current velocities, winter is the most energetic season, reaching values of up to 3.46 kWm^{-2}, with an average of 2.14 kWm^{-2}; in spring, the reduction in the velocity magnitude results in a significant decrease in the power density with an average value of 0.80 kWm^{-2}; finally, in summer and autumn the power density plummets due to the sharp reduction in the river discharges, both seasons presenting similar figures: 0.22 kWm^{-2} and 0.19 kWm^{-2}, respectively.

[FIGURE 10]

3.2. Site selection

The energy production of the SFT at the locations of interest is computed by combining the velocity magnitude results with the power curve of the turbine (Section 2) (Figure 11). As can be observed, the greatest energy output would be obtained in Area II, with an annual figure of 2.26 MWh, considerably higher than that in Area III (0.96 MWh) and tripling the value of Area I (0.73 MWh). Furthermore, the differences in energy production between areas differ markedly

during the year. The greatest differences are present in winter with a total energy production of 1.46 MWh, 0.62 MWh and 0.51 MWh at Areas II, III and I, respectively. In spring, a significant reduction in the energy production relative to the winter values occurs with total figures of 0.53 MWh, 0.26 MWh and 0.19 MWh at Areas II, III and I, respectively; thereby the differences between areas are accordingly smaller. Finally, in summer and autumn the energy output plummets, with each season representing in all cases less than 10% of the production attained in winter, and less than 30% of spring (e.g., the energy production during autumn at Area I would be 1.39% of the winter figure).

On the bases of these results, Area II emerges as the site with the greatest potential for installing a hydrokinetic turbine and therefore is retained for a thorough performance assessment.

[FIGURE 11]

3.3. Site-specific performance assessment

The following performance parameters of the SFT at Area II were computed: availability factor, A_f, capacity factor, C_f, and site-specific efficiency, η_{ss}, (Section 2), based on the intra-annual energy output results (Figure 12).

[FIGURE 12]

The good match between the operation requirements of the turbine and Area II, in particular its low cut-in velocity (0.7 ms^{-1}), leads to high values of the availability factor throughout the year: 100% in winter, 73.89% in spring, 49.86% summer, and 48.06% in autumn. These figures reflect the importance of the large river discharge in winter for the turbine performance, generating outflow currents in excess of 0.8 ms^{-1} throughout winter (even during the flood tide), and thus above the cut-in speed (0.7 ms^{-1}). The average annual availability factor is 67.95%, which corresponds to a total of 5871 hours of operational time in a year.

On the other hand, the capacity factor, C_f, is the parameter most influenced by the seasonality: 60.15% in winter, 22.06% in spring, 6.22% in summer, and 5.00% in autumn. From these values, the equivalent hours, E_h, (hours of energy production at nominal power) [35] are: 1299.24 h in winter, 476.50 h in spring, 134.35 h in summer, and 107.78 h in autumn. As a result, and despite the low levels attained over the second half of the year (summer-autumn), an annual value of 23.35% for the capacity factor, i.e., 2017 h of E_h, is achieved. These values are considered acceptable in the case of other renewables (e.g., C_f > 20% in wind energy) [48,49].

Finally, the site-specific turbine efficiency presents a completely different behaviour, with little seasonal variability: 40.18% in winter, 39.44% in spring, 40.16% in summer, 37.52% in autumn, meaning that the level of adequacy of the turbine for the site is roughly similar throughout the year.

3. Conclusions

The hydrokinetic resource in many coastal areas is not only the result of the tide, but also of other factors such as river discharges. As a case study of a fluvio-tidal coastal area, the Miño Estuary was considered in this work. With this aim, a shallow-water numerical model of the estuarine hydrodynamics, successfully validated against field measurements, was used to investigate the exploitation of the hydrokinetic resource in the estuary.

Three sites (Areas I, II and III) were initially selected as suitable for installing a third-generation SFT. The hydrological regime was found to produce a substantial seasonal variability. During winter and spring river discharges dominate the hydrodynamics, to the point of precluding the upstream flow during the flood throughout winter. In contrast, during summer and autumn, the reduction in freshwater discharges allows the tide to dominate the hydrodynamics. Then, the corresponding distribution of the power density was computed. It was found that the available resource experiences a significant intra-annual variation with average power density values during winter approximately ten times higher than during summer and autumn.

The most appropriate area for installing a hydrokinetic turbine amongst the three areas retained (I, II and III) was selected based on their seasonal energy production values. The largest energy

production can be obtained in Area II, almost doubling the energy output of Areas I and III; the seasonality, however, is considerable, with winter providing the lion's share of the energy production.

Finally, the intra-annual figures of several performance parameters of interest for the SFT-Area II combination were computed. All in all, from the results it can be concluded that the hydrodynamic regime of Area II is suited to the characteristics of the turbine selected, for which river discharges play a major role. In particular, its low cut-in velocity (0.7 ms^{-1}) leads to high values of the availability factor throughout the year, with an average annual figure of 67.95% and 100% in winter. Large river discharges during the rainy season (in winter and, to a lesser extent, spring) result in downstream currents above the cut-in velocity even during the flood tide, leading to high availability factors and, in general, good performance figures.

In sum, the results obtained indicate that in areas subject to both tidal effects and large river discharges, the performance of HECs may differ significantly from tide-dominated areas, with a substantial intra-annual variability that needs to be accounted for in planning the exploitation of the resource.

Acknowledgements

This paper has been conducted in the framework of the Research Project *Consolidación e estruturación* – 2016 CIGEO (Ref ED431B 2019/30) supported by Xunta de Galicia. The authors are grateful to the Instituto Hidrográfico de Portugal and to the Confederación Hidrográfica del Miño-Sil for providing the ADCP and river discharge data, respectively.

References

[1] World Commission on Environment and Development (WCED). Our Common Future. 1987.

[2] Aghsaee P, Markfort CD. Effects of flow depth variations on the wake recovery behind a horizontal-axis hydrokinetic in-stream turbine. Renewable Energy 2018;125:620-9.

371 [3] Els RHv, Junior ACPB. The Brazilian Experience with Hydrokinetic Turbines. Energy
372 Procedia 2015;75:259-64.
373 [4] Ramos V, Carballo R, Sanchez M, Veigas M, Iglesias G. Tidal stream energy impacts on
374 estuarine circulation. Energy Conversion and Management 2014;80:137-49.
375 [5] Petrie J, Diplas P, Gutierrez M, Nam S. Characterizing the mean flow field in rivers for
376 resource and environmental impact assessments of hydrokinetic energy generation sites.
377 Renewable Energy 2014;69:393-401.
378 [6] Holanda PdS, Blanco CJC, Mesquita ALA, Brasil Junior ACP, de Figueiredo NM, Macêdo
379 EN et al. Assessment of hydrokinetic energy resources downstream of hydropower plants.
380 Renewable Energy 2017;101:1203-14.
381 [7] European Commission. The exploitation of tidal marine currents. 1996;EUR16683EN.
382 [8] Zarzuelo C, López-Ruiz A, Díez-Minguito M, Ortega-Sánchez M. Tidal and subtidal
383 hydrodynamics and energetics in a constricted estuary. Estuarine, Coastal and Shelf Science
384 2017;185:55-68.
385 [9] Riglin J, Daskiran C, Jonas J, Schleicher WC, Oztekin A. Hydrokinetic turbine array
386 characteristics for river applications and spatially restricted flows. Renewable Energy
387 2016;97:274-83.
388 [10] Garcia Novo P, Kyozuka Y. Analysis of turbulence and extreme current velocity values in
389 a tidal channel. J Marine Sci Technol 2018.
390 [11] Segura E, Morales R, Somolinos JA, López A. Techno-economic challenges of tidal energy
391 conversion systems: Current status and trends. Renewable and Sustainable Energy Reviews
392 2017;77:536-50.
393 [12] King J, Tryfonas T. Tidal stream power technology - state of the art. Proceedings of IEEE
394 OCEANS 2009 - EUROPE Conference 2009:1-8.
395 [13] Núñez LR, López A, Somolinos JA. The GESMEY Project. Design and Development of a
396 Second Generation TEC. Proceedings of the 9th European Wave and Tidal Energy Conference
397 (EWTEC11) 2011.

[14] International Electrotechnical Commission. IEC-TC214, Technical Specification: Marine energy. Wave, tidal and other water current converters. Part 1: Terminology. IEC/TS 62600-1. 2011;1.0.

[15] Barbarelli S, Amelio M, Castiglione T, Florio G, Scornaienchi NM, Cutrupi A et al. Analysis of the equilibrium conditions of a double rotor turbine prototype designed for the exploitation of the tidal currents. Energy Conversion and Management 2014;87:1124-33.

[16] Rezanejad K, Guedes Soares C, López I, Carballo R. Experimental and numerical investigation of the hydrodynamic performance of an oscillating water column wave energy converter. Renewable Energy 2017;106:1-16.

[17] Vicinanza D, Contestabile P, Quvang Harck Nørgaard J, Lykke Andersen T. Innovative rubble mound breakwaters for overtopping wave energy conversion. Coastal Engineering 2014;88:154-70.

[18] López A, Somolinos JA, Núñez LR. Modelado Energético de Convertidores Primarios para el Aprovechamiento de las Energías Renovables Marinas. Revista Iberoamericana de Automática e Informática Industrial RIAI 2014;11:224-35.

[19] Wang W, Yin R, Yan Y. Design and prediction hydrodynamic performance of horizontal axis micro-hydrokinetic river turbine. Renewable Energy 2019;133:91-102.

[20] Li Y, Lence BJ, Calisal SM. An integrated model for estimating energy cost of a tidal current turbine farm. Energy Conversion and Management 2011;52:1677-87.

[21] Garcia Novo P, Kyozuka Y, Ginzo Villamayor MJ. Evaluation of turbulence-related high-frequency tidal current velocity fluctuation. Renewable Energy 2019;139:313-25.

[22] Arean N, Carballo R, Iglesias G. An integrated approach for the installation of a wave farm. Energy 2017;138:910-9.

[23] Vicinanza D, Contestabile P, Ferrante V. Wave energy potential in the north-west of Sardinia (Italy). Renewable Energy 2013;50:506-21.

[24] Weiss CVC, Ondiviela B, Guinda X, del Jesus F, González J, Guanche R et al. Co-location opportunities for renewable energies and aquaculture facilities in the Canary Archipelago. Ocean & Coastal Management 2018.

426 [25] Álvarez M, Carballo R, Ramos V, Iglesias G. An integrated approach for the planning of
427 dredging operations in estuaries. Ocean Engineering 2017;140:73-83.
428 [26] González-Caballín JM, Álvarez E, Guttiérrez-Trashorras AJ, Navarro-Manso A, Fernández
429 J, Blanco E. Tidal current energy potential assessment by a two dimensional computational fluid
430 dynamics model: The case of Avilés port (Spain). Energy Conversion and Management
431 2016;119:239-45.
432 [27] Garcia-Oliva M, Djordjević S, Tabor GR. The influence of channel geometry on tidal
433 energy extraction in estuaries. Renewable Energy 2017;101:514-25.
434 [28] Sousa R, Guilhermino L, Antunes C. Molluscan fauna in the freshwater tidal area of the
435 River Minho estuary, NW of Iberian Peninsula. International Journal of Limnology
436 2005;41(2):141-7.
437 [29] Freitas V, Costa-Dias S, Campos J, Bio A, Santos P, Antunes C. Patterns in abundance and
438 distribution of juvenile flounder Platichthys flesus, in Minho estuary (NW Iberian Peninsula).
439 Aquatic Ecology 2009;43:1143.
440 [30] Pugh DT. Tides, Surges, and Mean Sea-Level/a Handbook for Engineers and Scientists. :
441 John Wiley & Sons Inc, 1996.
442 [31] Fouz DM, Carballo R, Iglesias G. Tidal stream energy production in estuarine areas: A
443 case study in NW Spain. Abstract Volume Campus do Mar International Science Conference
444 2018 2018:24.
445 [32] Deltares. User Manual Delft3D-FLOW. Deltares ed. Delft, The Netherlands, 2010.
446 [33] Carballo R, Iglesias G, Castro A. Numerical model evaluation of tidal stream energy
447 resources in the Ría de Muros (NW Spain). Renewable Energy 2009;34:1517-24.
448 [34] Blunden LS, Bahaj AS. Initial evaluation of tidal stream energy resources at Portland Bill,
449 UK. Renewable Energy 2006;31:121-32.
450 [35] Ramos V, Iglesias G. Performance assessment of Tidal Stream Turbines: A parametric
451 approach. Energy Conversion and Management 2013;69:49-57.
452 [36] Zarzuelo C, López-Ruiz A, Ortega-Sánchez M. Impact of human interventions on tidal
453 stream power: The case of Cádiz Bay. Energy 2018;145:88-104.

[37] Le Provost C, Bennett AF, Cartwright DE. Ocean tides for and from Topex/Poseidon. Science 1995;267:639-47.

[38] Iglesias G, Sánchez M, Carballo R, Fernández H. The TSE index – A new tool for selecting tidal stream sites in depth-limited regions. Renewable Energy 2012;48:350-7.

[39] Iglesias G, Carballo R. Seasonality of the circulation in the Ría de Muros (NW Spain). J Mar Syst 2009;78:94-108.

[40] Loutas TH, Sotiriades G, Kostopoulos V. On the application of wavelet transform of AE signals from composite materials. 2004:433-45.

[41] Daubechies I. Orthonormal bases of compactly supported wavelets. Communications in Pure and Applied Mathematics 1988;XLI:901-96.

[42] Hu X-, Liu LT, Ducarme B, Hsu HT, Sun H-. Wavelet filter analysis of local atmospheric pressure effects in the long-period tidal bands. Phys Earth Planet Inter 2006;159:59-70.

[43] Chow VT. Open-channel hydraulics. New York: McGraw-Hill, 1959.

[44] Bahaj AS. Generating electricity from the oceans. Renewable and Sustainable Energy Reviews 2011;15:3399-416.

[45] Ramos V, Carballo R, Álvarez M, Sánchez M, Iglesias G. A port towards energy self-sufficiency using tidal stream power. Energy 2014;71:432-44.

[46] Chang T, Wu Y, Hsu H, Chu C, Liao C. Assessment of wind characteristics and wind turbine characteristics in Taiwan. Renewable Energy 2003;28:851-71.

[47] Carballo R, Iglesias G. A methodology to determine the power performance of wave energy converters at a particular coastal location. Energy Conversion and Management 2012;61:8-18.

[48] Boccard N. Capacity factor of wind power realized values vs. estimates. Energy Policy 2009;37:2679-88.

[49] Nemes C, Munteanu F. The wind energy system performance overview: Capacity factor vs. technical efficiency. Int J Math Models Methods Appl Sci 2011;5:159-66.

Figure captions

Figure 1. Location of the Miño Estuary on the Galician coast, NW Spain.

Figure 2. Miño Estuary, study area and ADCP location.

Figure 3. Area covered by the model grid.

Figure 4. Bathymetry and topographic configuration of the Miño Estuary as interpolated to model grid.

Figure 5. Magnitude of current velocities measured by the ADCP (circles) and computed by the model (line) projected along the main axis of the estuary during the validation period.

Figure 6. Power curve of SFT.

Figure 7. Magnitude of the current velocity at Area I throughout a 14.75-day spring-neap cycle in the winter, spring, summer and autumn cases.

Figure 8. Magnitude of the current velocity at Area II throughout a 14.75-day spring-neap cycle in the winter, spring, summer and autumn cases.

Figure 9. Magnitude of the current velocity at Area III throughout a 14.75-day spring-neap cycle in the winter, spring, summer and autumn cases.

Figure 10. Power density at Area II throughout a 14.75-day spring-neap cycle in the winter, spring, summer and autumn cases.

Figure 11. Annual electric energy output of SFT at Areas I, II and III.

Figure 12. Performance of SFT at Area II in terms of availability factor, capacity factor and site-specific turbine efficiency.

Table 1. Tidal constituents at the ocean boundary of the grid.

Constituent	Amplitude (m)	Phase (º)
M2	1.0654	76.5400
S2	0.3700	105.9200
N2	0.2251	57.5200
K2	0.1017	102.1200
K1	0.0743	66.2800
O1	0.0595	320.7100
P1	0.0215	57.5100
Q1	0.0195	265.4700
Z0	2.0687	0.0000

Table 2

Table 2. Case studies.

Season	Months	Average discharge (m^3s^{-1})	Average temperature (^oC)
Winter	January February March	1013.25	10.9
Spring	April May June	568.47	14.5
Summer	July August September	174.09	20.5
Autumn	October November December	129.21	14.9

Table 3

Table 3. Main technical specifications of SFT [D (m), rotor diameter; A (m^2), swept area; W (kg), turbine weight; V_{ci} (ms^{-1}), cut-in velocity; V_{co} (ms^{-1}), cut-off velocity; V_R (ms^{-1}), rated velocity; P_R (kW), rated power; L (m), device length; B (m), device width; H (m), device height; N, number of blades; ω (rpm), angular velocity].

Smart Freestream turbine			
D (m)	1.0	P_R (kW)	1.12
A (m^2)	0.8	L (m)	2.6
W (kg)	300.0	B (m)	1.1
V_{ci} (ms^{-1})	0.7	H (m)	1.1
V_{co} (ms^{-1})	3.1	N	3.0
V_R (ms^{-1})	2.0	ω (rpm)	90-230

Figure 1

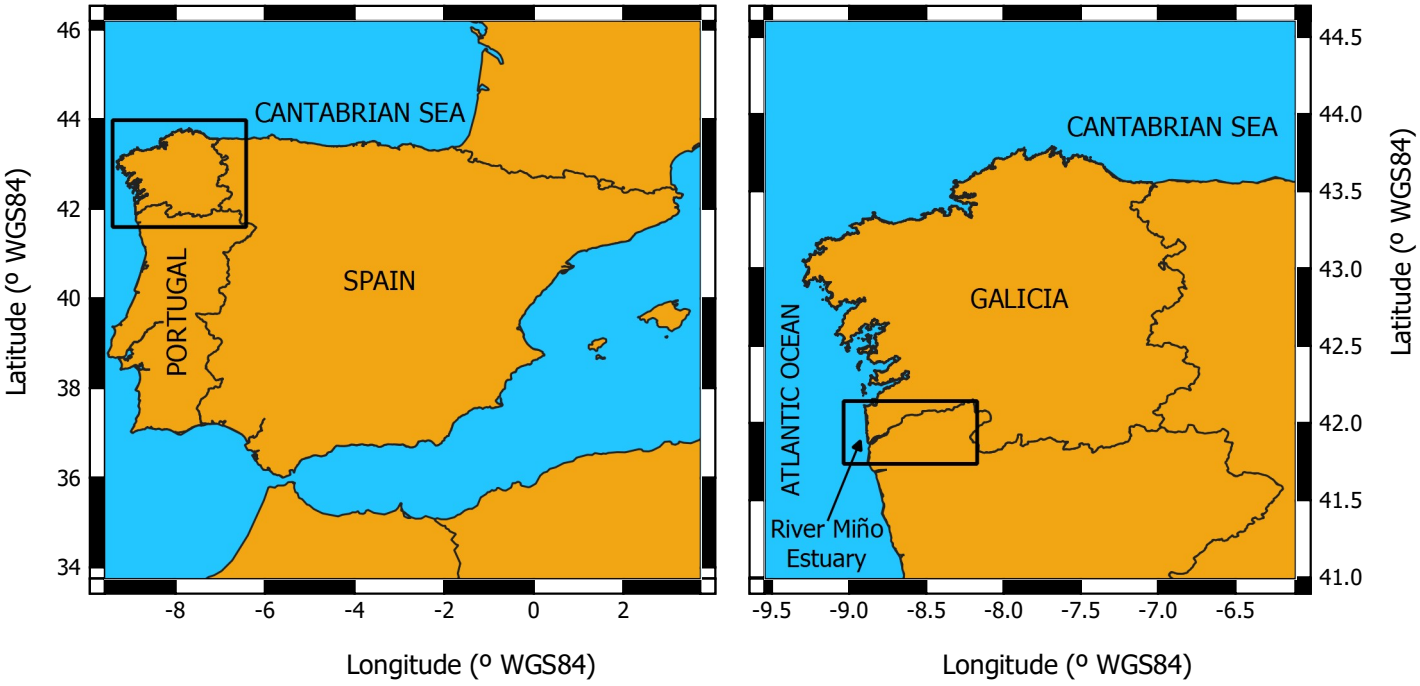

CANTABRIAN SEA
SPAIN
PORTUGAL
Latitude (º WGS84)
Longitude (º WGS84)
CANTABRIAN SEA
GALICIA
ATLANTIC OCEAN
River Miño
Estuary
Latitude (º WGS84)
Longitude (º WGS84)

Figure 2

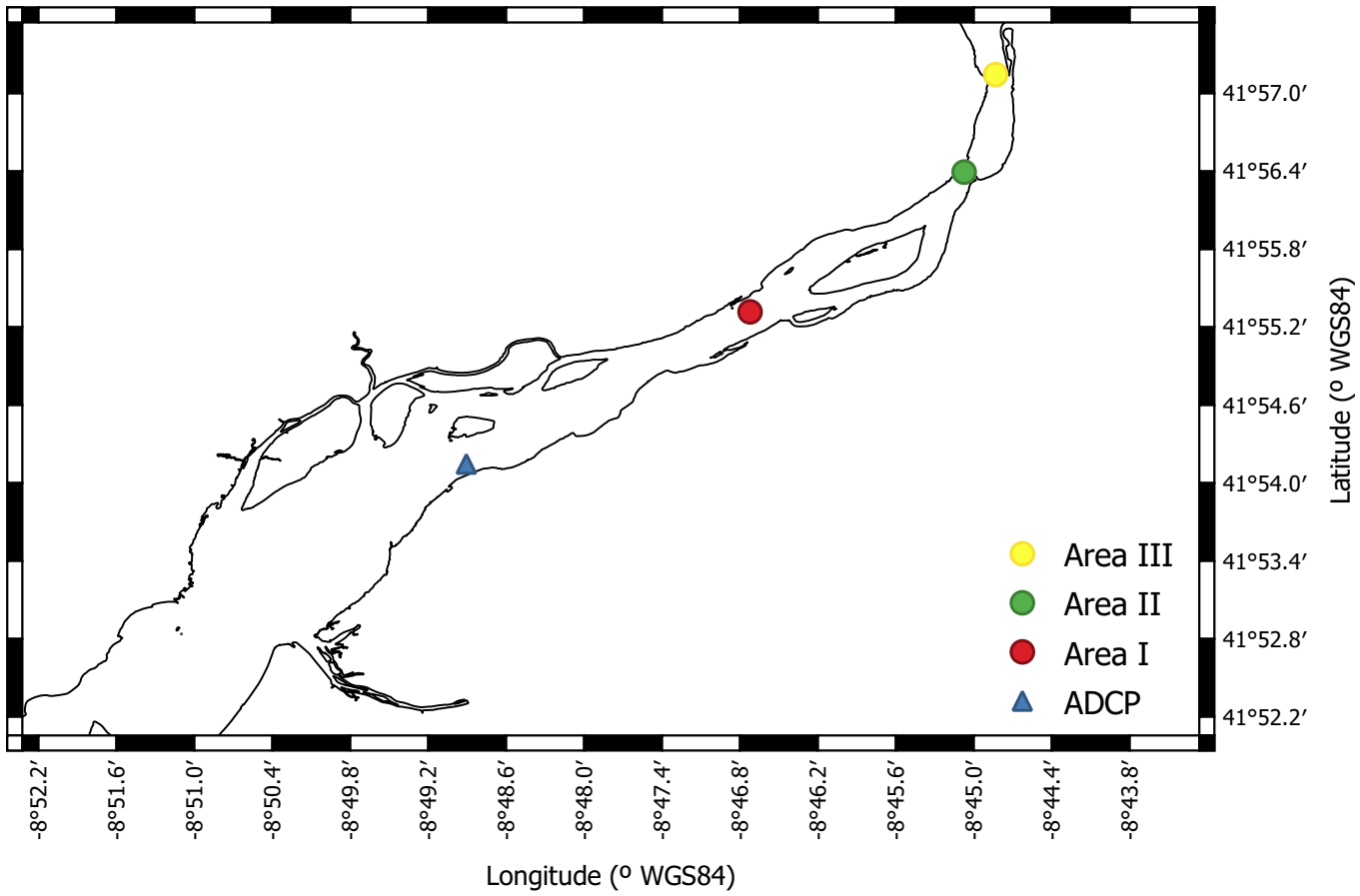

41°57.0′
41°56.4′
41°55.8′
41°55.2′
41°54.6′
41°54.0′
41°53.4′
41°52.8′
41°52.2′
Latitude (º WGS84)
Area III
Area II
Area I
ADCP
-8°52.2′
-8°51.6′
-8°51.0′
-8°50.4′
-8°49.8′
-8°49.2′
-8°48.6′
-8°48.0′
-8°47.4′
-8°46.8′
-8°46.2′
-8°45.6′
-8°45.0′
-8°44.4′
-8°43.8′
Longitude (º WGS84)

Figure 3

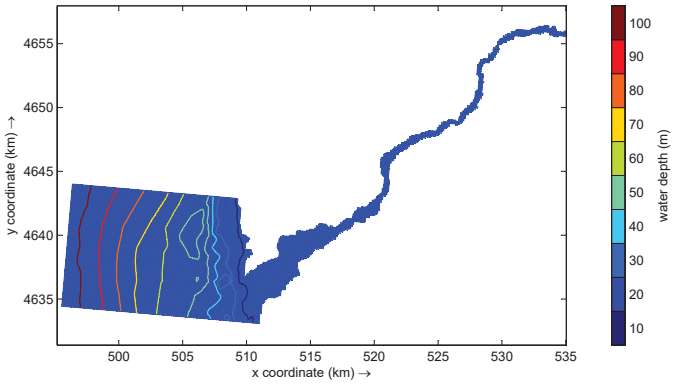

4655
4650
4645
4640
4635
y coordinate (km) →
500
505
510
515
520
525
530
535
x coordinate (km) →
100
90
80
70
60
50
40
30
20
10
water depth (m)

Figure 4

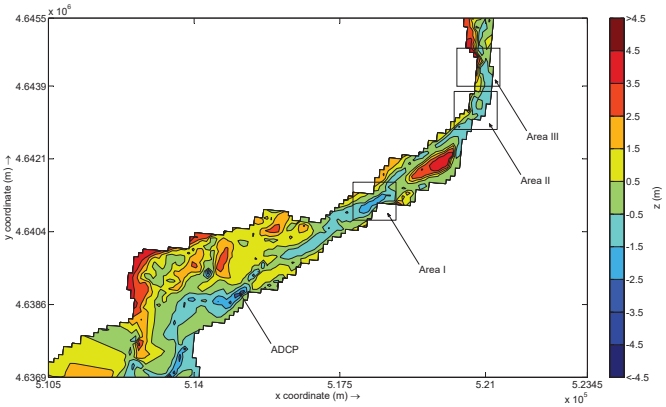

x 10^6
4.6455
4.6439
4.6421
4.6404
4.6386
4.6369
y coordinate (m) →
5.105
5.14
5.175
5.21
5.2345
x 10^5
x coordinate (m) →
Area III
Area II
Area I
ADCP
>4.5
4.5
3.5
2.5
1.5
0.5
-0.5
-1.5
-2.5
-3.5
-4.5
<-4.5
z (m)

Figure 5

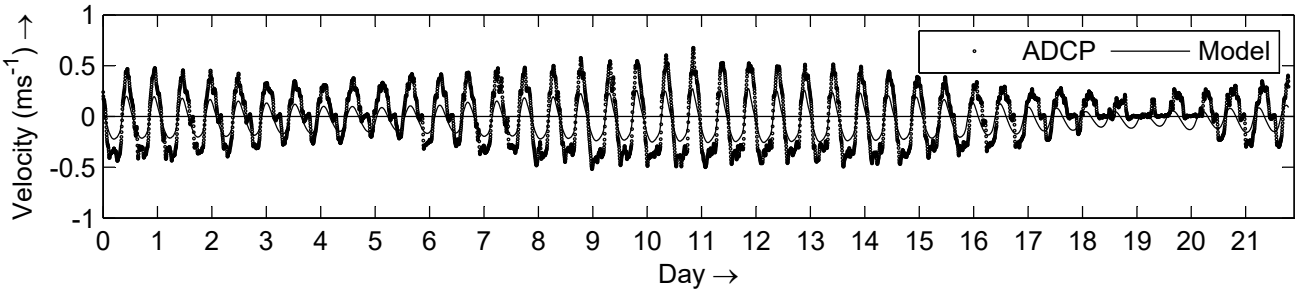

ADCP
Model
Velocity (ms-1) →
Day →
1
0.5
0
-0.5
-1
0 1 2 3 4 5 6 7 8 9 10 11 12 13 14 15 16 17 18 19 20 21

Figure 6

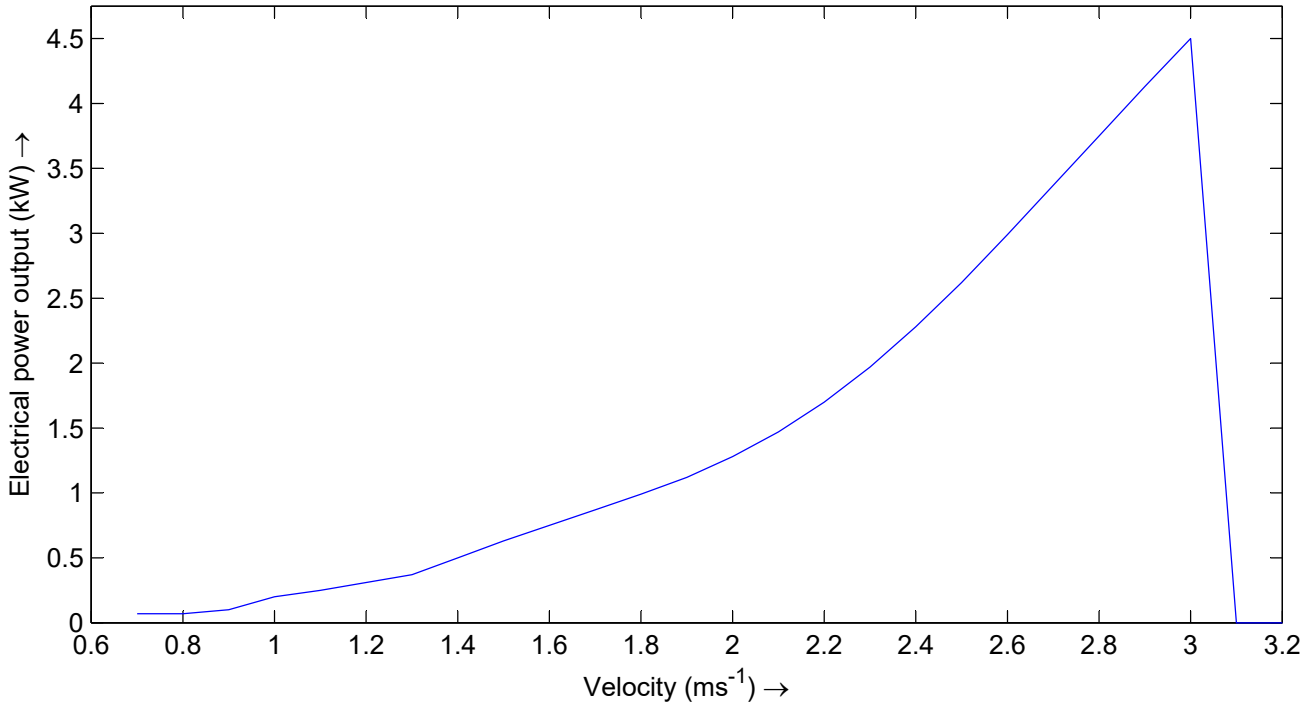

Electrical power output (kW) →
4.5
4
3.5
3
2.5
2
1.5
1
0.5
0
0.6
0.8
1
1.2
1.4
1.6
1.8
2
2.2
2.4
2.6
2.8
3
3.2
Velocity (ms-1) →

Figure 7

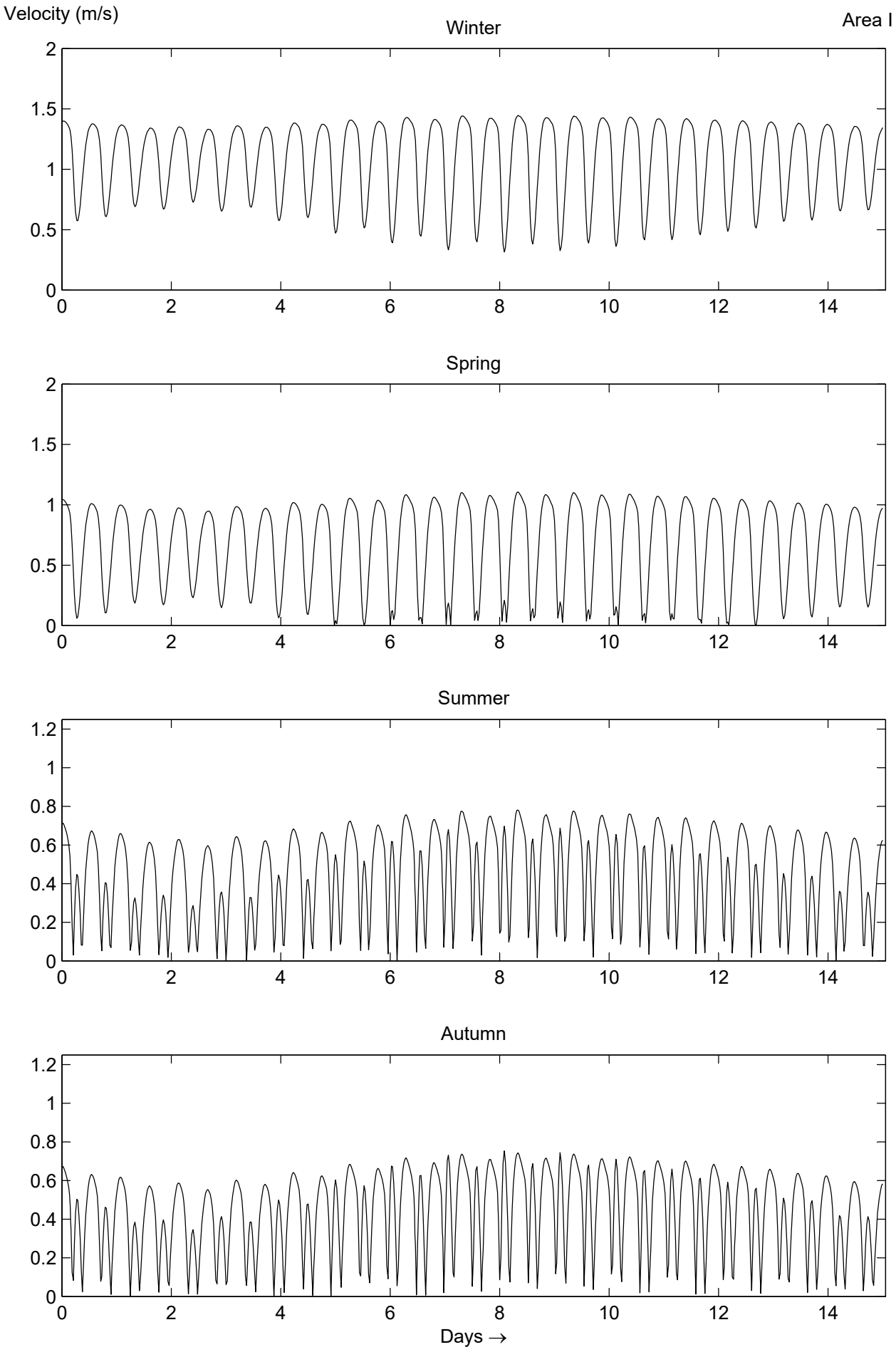


Figure 8

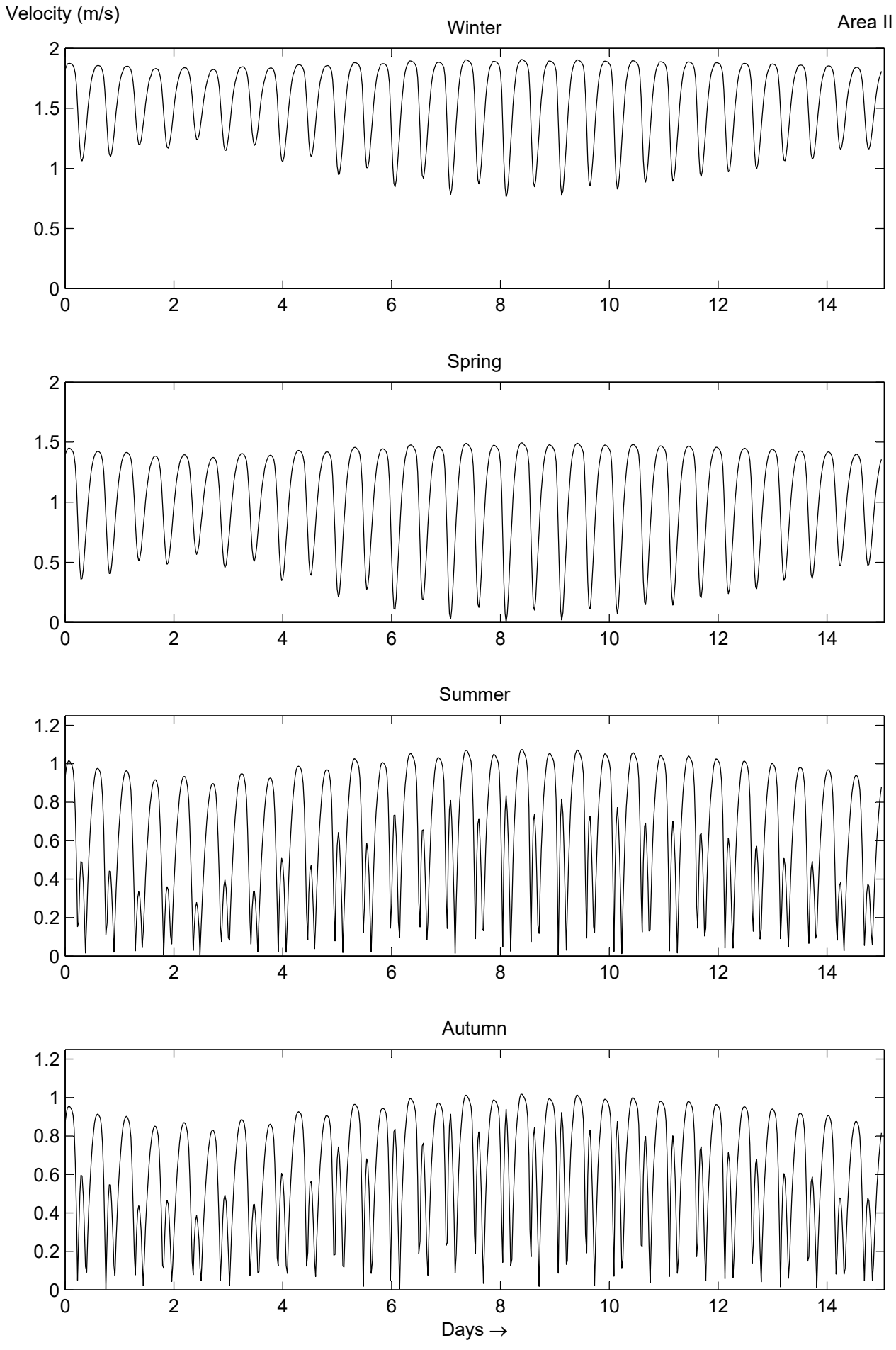


Figure 9

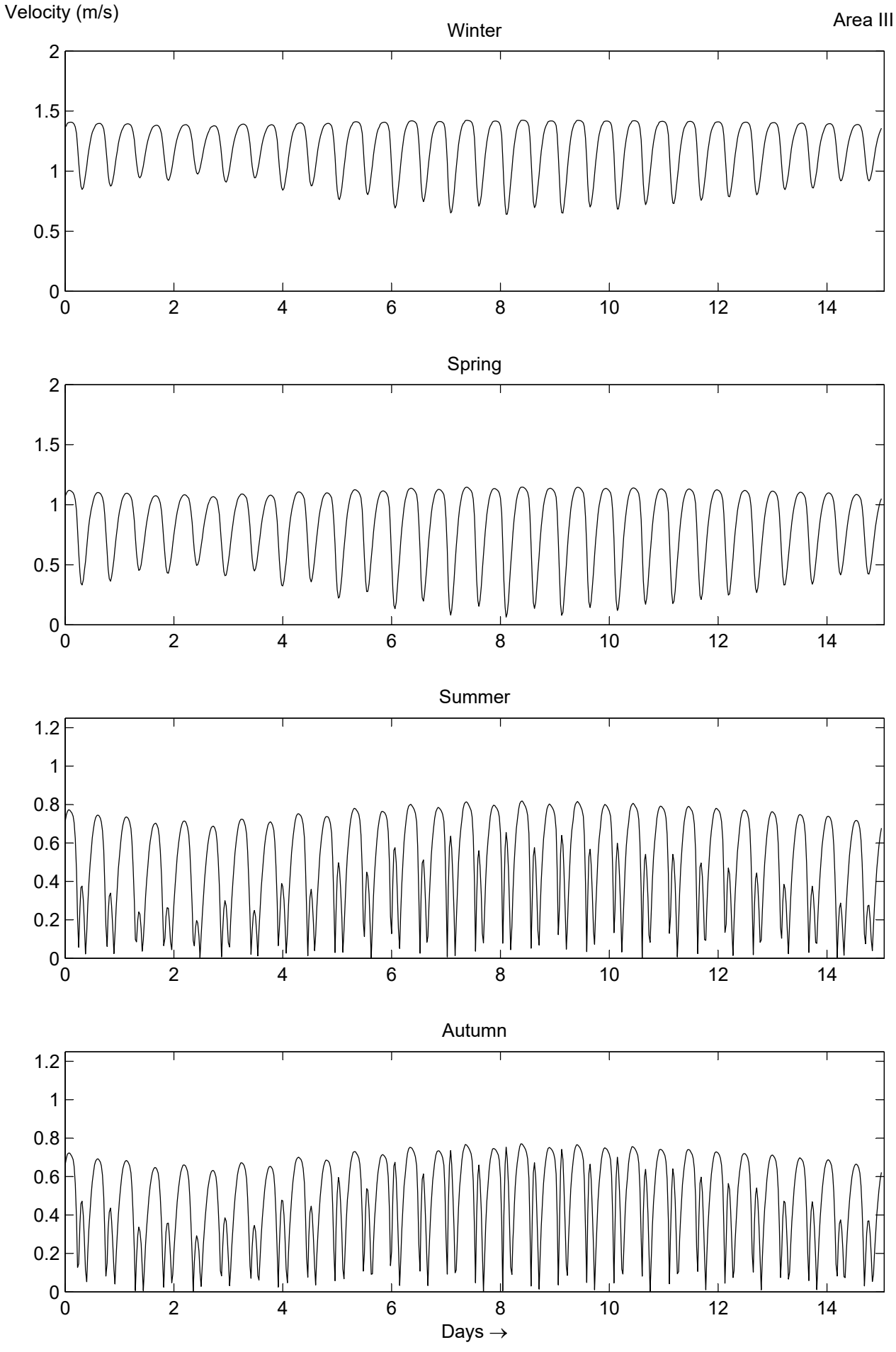


Figure 10

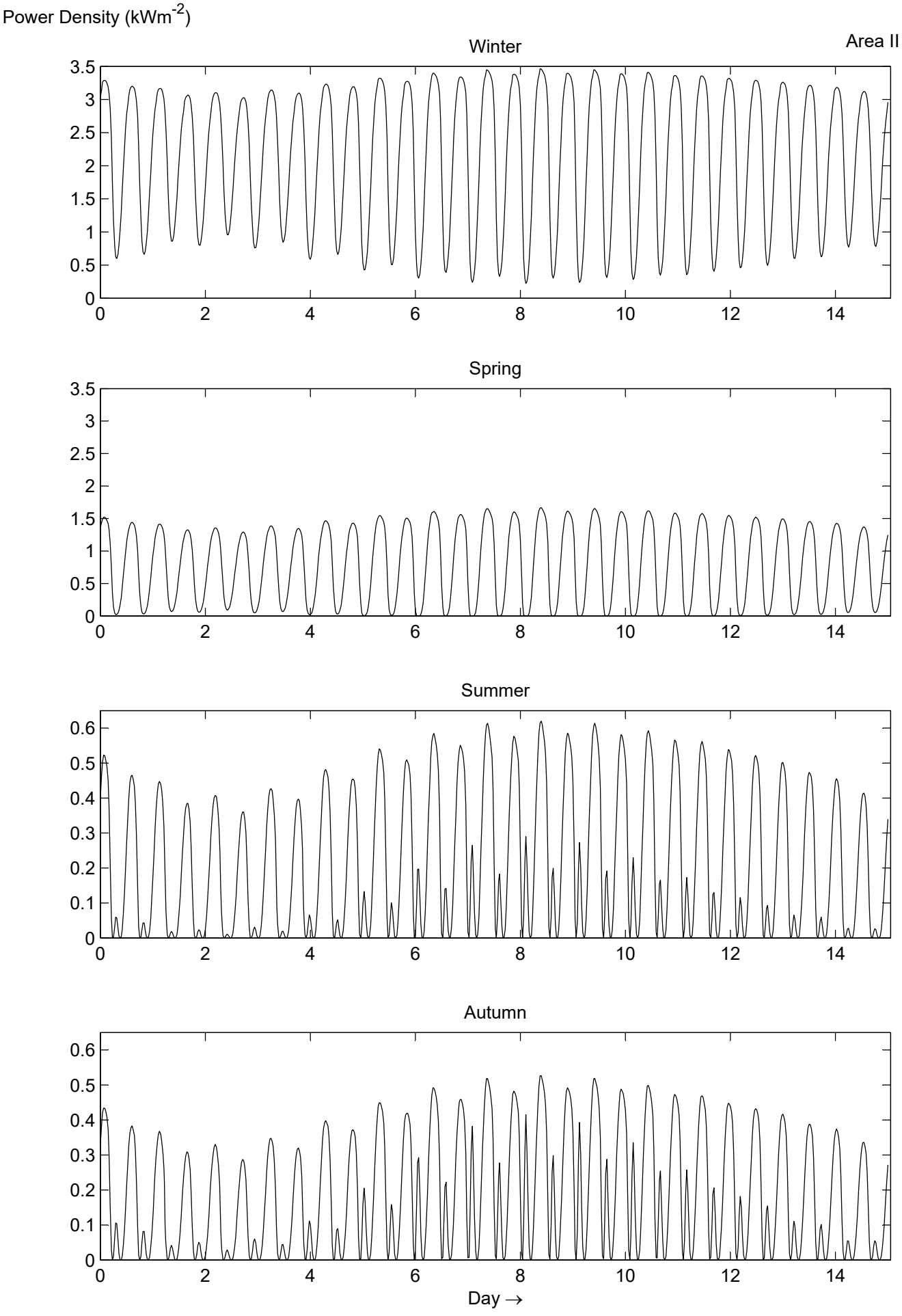


Figure 11

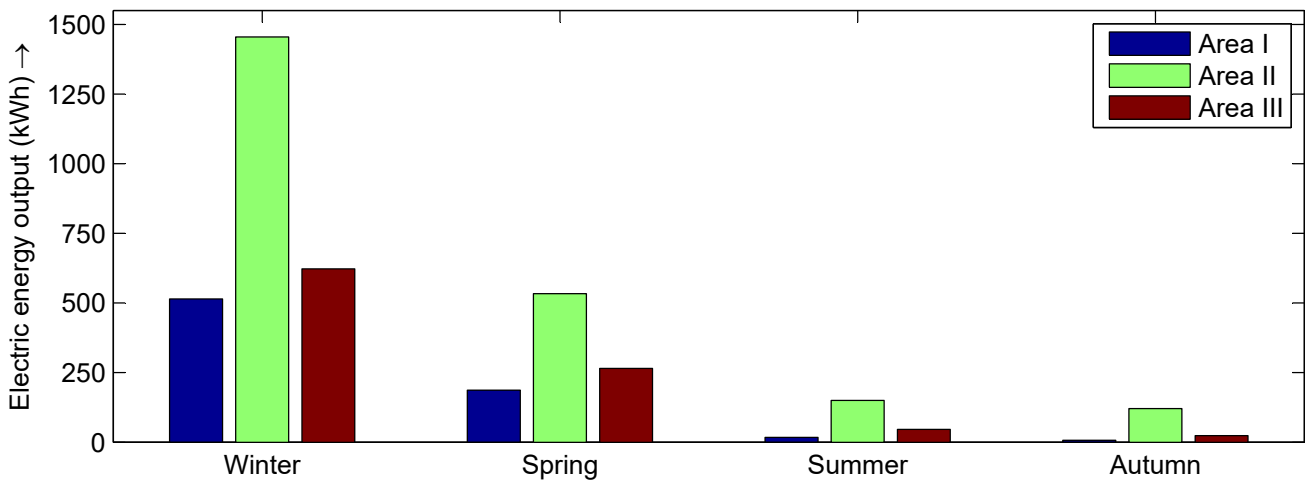
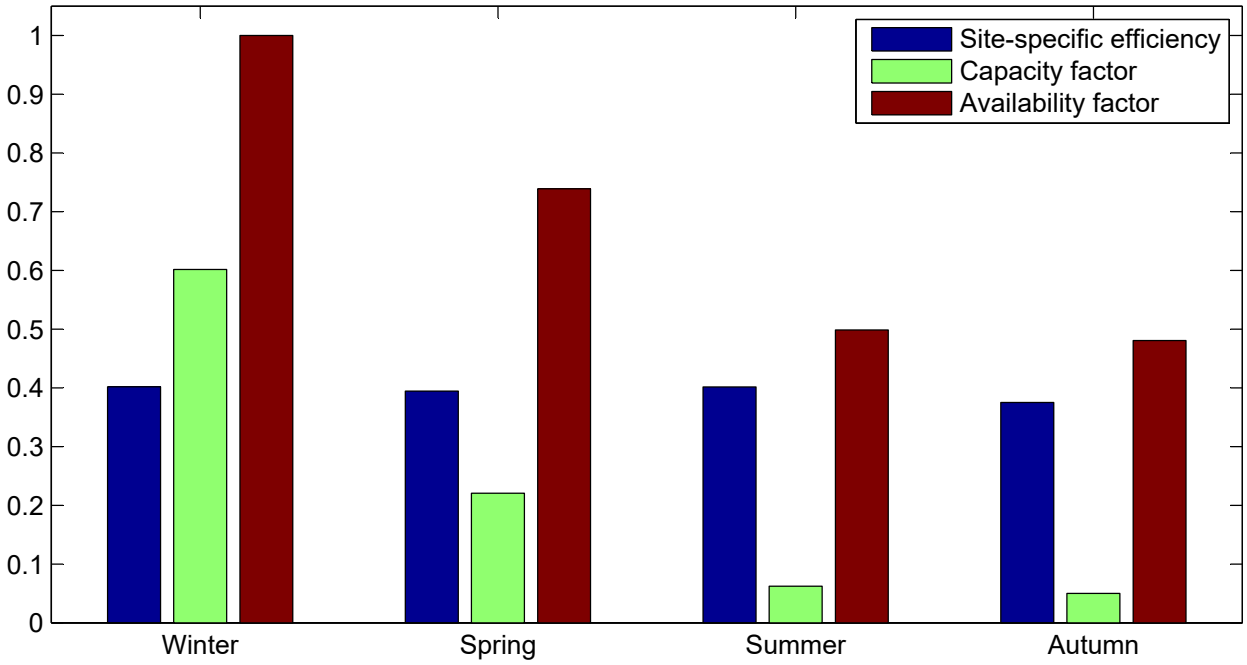

Electric energy output (kWh) →
1500
1250
1000
750
500
250
0
Winter
Spring
Summer
Autumn
Area I
Area II
Area III

Figure 12


Site-specific efficiency
Capacity factor
Availability factor
1
0.9
0.8
0.7
0.6
0.5
0.4
0.3
0.2
0.1
0
Winter
Spring
Summer
Autumn